Anisotropic Properties of the Earth's Velocity Structure in Shikoku Island, Japan: Insights from Receiver Function Analysis and Shear Wave Splitting

Yihuan Ruan[1], Yoshihiro Ito[2], and Yasunori Sawaki[1,3]

[1]Graduate School of Science, Kyoto University, Gokasho, Uji 611-0011, Japan

[2]Disaster Prevention Research Institute, Kyoto University, Gokasho, Uji 611-0011, Japan

[3]Now at Geological Survey of Japan, National Institute of Advanced Industrial Science and Technology (AIST), Tsukuba Central 7, 1-1-1 Higashi, Tsukuba 305-8567, Japan

Corresponding author: Yihuan Ruan (ruan.yihuan.86s@st.kyoto-u.ac.jp)

Key Points:

- Fine-resolution anisotropic property calculated above the oceanic crust in Shikoku Island, southwest Japan, by receiver function analysis.
- Weaker anisotropic strength in tectonic tremor-clustered areas, especially northwestern Shikoku, where the mantle wedge is serpentinized.
- Serpentinization of the mantle and metasomatic reactions lead to hydrofracturing and relatively low anisotropic strength.

Abstract

The anisotropic properties of the Earth's velocity structure can be revealed through a combination of receiver function (RF) analysis and shear wave splitting. The splitting parameters, fast polarization direction (FPD) and split time, are used to infer the anisotropic properties. We utilized seismograms from stations on Shikoku Island, Japan, and applied the Bayesian information criterion to constrain the model size of the RF. We showed different anisotropic properties between northern and southern areas corresponding to the Median Tectonic Line. In the southern part, the FPDs were sub-perpendicular to the plunge of the subducting slab, while in the northern part, the FPDs were sub-parallel to the plunge of the slab. Our results indicate that anisotropic strengths are weaker in the tectonic tremor-band in northwestern Shikoku and stronger in the northern part of central and eastern Shikoku around the no-tectonic-tremor area. These anisotropic variations may reveal the geological structure under Shikoku Island.

Plain Language Summary

Receiver function (RF) analysis is sensitive to impedance discontinuity as it can extract converted shear waves from seismograms. In this study, a relatively precise anisotropy was estimated by including a high-frequency component and combining it with shear wave splitting. The Bayesian information criterion was used to control the model size of RF, which consists of a series of spikes generated by time-domain iterative deconvolution. The direction of the resulting anisotropy agrees with the strike of the subducting Philippine Sea Plate in southern Shikoku. In the more northern area, the direction is sub-parallel to the plunge of the subducting slab (N–S). Additionally, the delay time between fast and slow shear waves indicates the strength of anisotropy in this study. In the tectonic tremor-clustered area in northwestern Shikoku, the strengths of anisotropy are regionally weaker than those in other areas. Moreover, stronger anisotropy was measured in the deeper northern part of central and eastern Shikoku, with no tectonic tremor activity. As several factors contribute to the anisotropy, the resulting anisotropy may reflect the structure, including the subducting slab, continental crust, and even the mantle wedge.

1 Introduction

Anisotropic properties of seismic wave propagation provide important information for understanding the Earth's seismotectonic and tectonic evolution. Lattice preferred orientation (LPO) and extensive-dilatancy anisotropy (EDA) are commonly used to explain the seismic wave anisotropy. These properties are frequently attributed to the LPO of minerals (Hess, 1964). For example, olivine can exhibit five different types of anisotropy depending on the water content, pressure, and temperature (Karato et al., 2008). Another interpretation of anisotropy in seismology is the preferred orientation of cracks within the crust. Many studies have shown that microcracks and fractures tend to be aligned perpendicular to the direction of the minimum compressional stress (e.g., Crampin & Peacock, 2005; Huang et al., 2011; Silver & Chan, 1991). Below the critical depth of approximately 500–1000 m, the increased vertical lithostatic pressure causes the nearly vertical propagation to show a faster velocity in the strike of the crack direction, which is sub-parallel to the maximum horizontal stress (S_{hMax}) (Crampin & Peacock, 2005). This alignment of microcracks induced by tectonic stress and the lineament structure is called EDA (Crampin et al., 1984; Iidaka et al., 2014).

Seismic anisotropy results can be influenced by plate subduction, especially in the wedge mantle, which is a wedge-shaped region that lies between the subducting oceanic plate and the overlying continental plate. This region plays a crucial role in subduction zone dynamics and the generation of earthquakes and volcanoes. Olivine and serpentine are minerals that mainly contribute to anisotropy in subduction zones (Lassak et al., 2006; Shiomi & Park, 2008; Wang et al., 2019). Olivine, which is the upper mantle's most abundant mineral, was considered to be the primary contributor to anisotropy (Silver & Chan, 1991). The serpentinized mantle wedge also exists in the subduction system. Anisotropy is expected to be trench-parallel and trench-normal above the steep and flatter subducting plates, respectively, as the mineral's geometry is projected onto the horizontal plane differently in each case (Katayama et al., 2009). Moreover, the subduction zone's complexity may trigger slow earthquakes along the locally serpentinized plate interface, potentially influenced by pore pressure buildup (Katayama et al, 2013).

The Philippine Sea (PHS) Plate is subducted under the Eurasian Plate at a velocity of 4–5 $cm \cdot yr^{-1}$ (Seno et al., 1993). Previous studies have measured the geometry of the subducting PHS Plate beneath Shikoku Island (Hirose et al., 2008; Ito et al., 2009; Shiomi et al., 2006, 2020; Ueno et al., 2008;). Based on their results, as the plate is subducted, the PHS Plate dips gently at

approximately 6° from the Nankai trough to central Shikoku, and the dip angle steepens toward the north (Ito et al., 2009). In western Shikoku, the PHS Plate maintains a dipping angle of approximately 8–10° and is in contact with the continental lower crust beneath the middle and southern portions of Shikoku. The 30-km iso-depth line of the top surface of the PHS Plate is generally considered a rough dividing line between the northern and southern regions of Shikoku Island (Figure 1). By contrast, the PHS Plate subducts beneath the wedge mantle in the northern area (e.g., Nakanishi et al., 2018) and the most active slow-earthquake areas in the world (e.g., Obara & Kato, 2016; Obara, 2002). Additionally, the Median Tectonic Line (MTL), the longest fault system in Japan, is located at Shikoku.

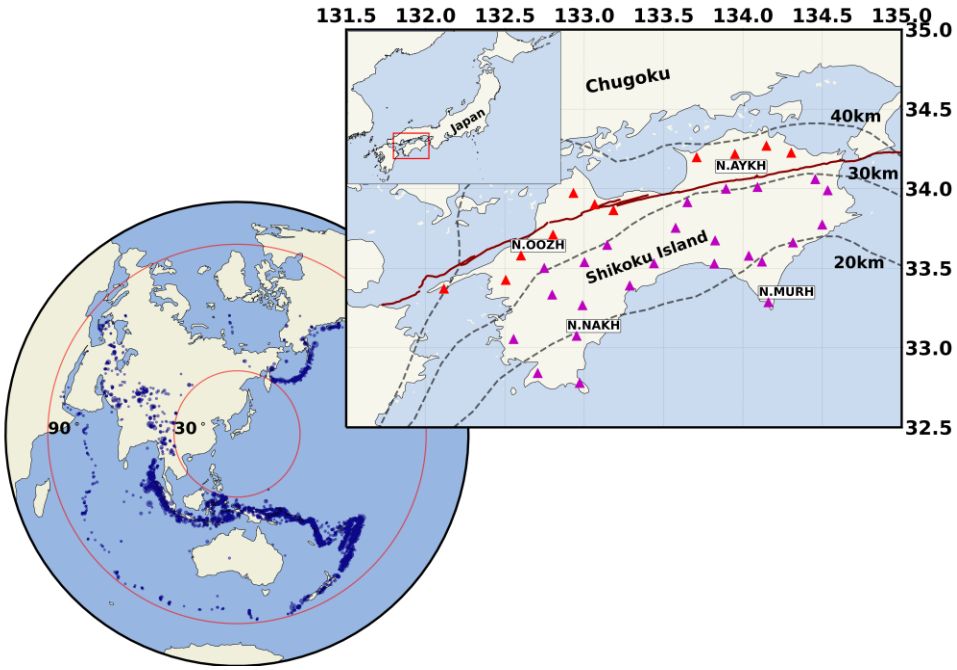

Figure 1. Epicenter distribution of teleseismic events and stations used in this study. The triangles depict the Hi-net and F-net stations in the northern and southern Shikoku Island (red and magenta, respectively). The dark red lines indicate MTL. The dashed lines indicate the top interface of the PHS Plate by Hirose et al. (2008).

Several previous studies have investigated the anisotropic properties beneath Shikoku Island. Anisotropy tomography of S-waves in the crust revealed that fast polarization directions (FPDs) are sub-parallel to the trajectories of maximum horizontal compression in the NW–SE direction (Ishise & Oda, 2009). The present study suggests that the FPDs revealed from *Ps*

phases on receiver functions (RFs) reflect the anisotropic properties in the upper crust and are aligned with the direction of S_{hMax} (Nagaya et al., 2011).

The occurrence of tectonic tremors beneath the northern part of Shikoku Island exhibits lateral variation, particularly in terms of the accumulated total energy over a decade (Annoura et al., 2016). The area with the highest energy release due to tectonic tremors is situated in the western section of Shikoku Island, whereas it is comparatively lower in the eastern end and middle of the Island. Although tectonic tremors have shown lateral variation on Shikoku Island, the seismic anisotropic structures of the entire island, especially in the wedge mantle, have not been thoroughly investigated and compared. As the fast axes of splitting shear waves reflect structural properties, such as EDA and fractured fault system in the crust and LPO in the mantle, we investigated the anisotropic properties and their spatial variation throughout Shikoku Island, considering the geological structure. In particular, we adopted simultaneous analysis of RFs and shear wave splitting to estimate the seismic anisotropic structure and compare the lateral variation of slow earthquake activity on Shikoku Island.

2 Data and Methods

2.1 Seismic record dataset

We utilized seismic records obtained from a high-sensitivity seismograph network (Hi-net) and a broadband seismograph network (F-net) (National Research Institute for Earth Science and Disaster Resilience, 2019a, 2019b)(Figure 2). An average of 166 seismograms at each station were selected from the U.S. Geological Survey earthquake catalog (USGS, 2022) and filtered at 0.1–20 Hz. Only high signal-to-noise ratio teleseismic records with M ≥5.8 for epicenters between 30° and 90 °were used for RF calculation. We corrected the horizontal sensor orientations of the Hi-net seismograms (Shiomi, 2013) and rotated the seismograms to the *LQT*-coordinate system. Based on the power spectral density of each cut component calculated for both the signal and noise windows (seismic record before *P* phase arrival), we applied a Gaussian low-pass filter at 1 Hz with a 3-dB cutoff using a Gaussian factor of 5.5.

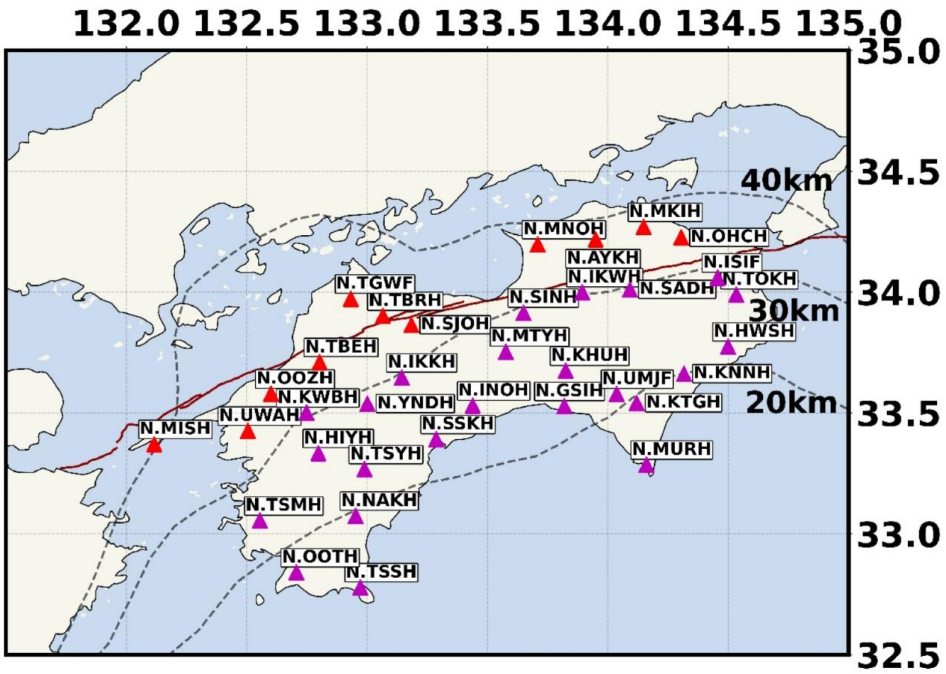

124 **Figure 2.** Hi-net and F-net stations in northern and southern Shikoku Island, marked using red
125 and magenta, respectively.

126 ***2.2 Bayesian information criterion (BIC) incorporation into the time-domain iterative***
127 ***deconvolution method***

128 According to a study by Ligorría and Ammon (1999), RFs calculated using the time-
129 domain iterative deconvolution method typically exhibit numerous spikes, with each spike
130 representing a converted *Ps* phase. However, the iterative procedure can continue generating
131 spikes until a predetermined condition is met, based on the difference between adjacent squared
132 errors (δε). To better control the size of the resulting model (i.e., the number of spikes), we
133 propose a new conditional judgment based on the BIC.

134 Schwarz (1978) derived BIC as

135 $$BIC = -2\,ln(L) + K\,ln(n) \quad (1)$$

136 where L indicates the maximized value of the likelihood function for the estimated model
137 under the assumption that the error or disturbance of the data follows a normal distribution; K is
138 the number of estimable parameters in the approximating model, which means spike number in
139 the iterative deconvolution receiver function method; n is the size of samples. The maximized

value of the likelihood function L can be expressed as the averaged least sum of the squared residuals, $\hat{\sigma}^2$. Then, Eq. 1 can be written as

$$BIC = n\,ln(\hat{\sigma}^2) + K\,ln(n)$$
$$\hat{\sigma}^2 = \frac{\sum(\varepsilon_i)^2}{n} \quad (2)$$

where ε_i is the estimated residual from the fitted model at each point. Then the "suitable" RF will have the minimum BIC value under the assumption that the error or disturbance of data follows normal distribution.

Silver and Chan (1991) also proposed a method to estimate the uncertainty of the grid search results. It is assumed that the signal is combined with Gaussian white noise and obeys the F distribution, as follows:

$$\frac{\left(E_t(t,\varphi,\delta t) - E_t^{\min}\right)/k}{E_t^{\min}/(v-k)} \sim F_{k,v-k} \quad (3)$$

Here, E_t indicates the summation of the squared T-component energy and k=2 indicates two free parameters. A quarter of the width and length of the confidence interval indicates the standard error. The confidence interval for (φ, δt) is defined as

$$\frac{E_t(t,\varphi,\delta t)}{E_t^{\min}} \le 1 + \frac{k}{v-k} F_{k,v-k}(1-\alpha) \quad (4)$$

Here, α = 0.05 decides the confidence level (95% confidence interval). In particular, v indicates the degree of freedom, and we followed the corrected formulae rederived by Walsh et al. (2013) for its calculation of grid search uncertainty in our results.

2.3 Shear-wave polarization anisotropy from receiver function

The RF can extract the *Ps*-waves converted at the *S*-wave velocity discontinuities beneath a seismic station. The *Ps*-waves contain anisotropic properties only above the discontinuities, whereas the splitting properties of teleseismic *S*-waves or *SKS*-waves also reflect deeper structures, such as the mantle. The splitting patterns from *Ps*-waves are more reliable for constraining crustal anisotropic structures.

163 *S*-wave anisotropy on RFs contributes to the *Q*- and *T*-components of the RFs, just as the
164 azimuth of incidence generates a different pattern. Regarding the back-azimuthal variation,
165 mainly the four-lobed and two-lobed patterns are shown in the RFs, which are caused by the
166 horizontal anisotropic symmetry and tilt anisotropic symmetry axes, or the dipping interface,
167 respectively.

168 Because of the complexity of the converted *S*-wave pattern in the RFs, determining the
169 azimuths of the FPD (φ) and the delay times (δt) of the split shear waves by a single RF trace
170 will be biased. Therefore, we gathered all RF traces over the back azimuth and analyzed them
171 simultaneously by considering the present pattern from all factors. The time window was
172 selected through a manual visual check on *L*-component RFs to include as many specific phases
173 as possible, similar to previous works (e.g., Silver & Chan, 1991). The objective function of
174 traditional grid search (φ, δt) becomes seeking the "best" parameter pair that minimizes the total
175 *T*-component energy of all traces in the previous method.

176 To verify the performance of combination of sorted RFs and shear wave splitting
177 methods, we conducted a simple synthetic tests for measuring the anisotropic medium with
178 dipping interface (Table 1 and Figures 3 and 4). The anisotropic patterns generated by tilt
179 interface were eliminated after splitting analysis (Figure 3b). Synthetic results demonstrate that
180 this method effectively eliminates the energy pattern resulting from dipping interfaces and
181 produces reliable results even in cases of limited back-azimuth coverage. Specifically, we found
182 that this approach yields a standard error <20° for back-azimuth coverage and 0.15 s for both
183 FPD and delay time.

Table 1. Assumed model for the receiver function synthetic test

Layer	Thickness [km]	V_P [km/s]	V_S [km/s]	Density [g/cm^3]	Anisotropy	Fast axis	Top Interface			
					%P	%S	Trend [°]	Plunge [°]	Dip [°]	Strike [°]
1	20	6.3	3.7	2.75	5	5	30	0	-	-
2	-	7.8	4.3	3.25	0	0	-	-	12	0

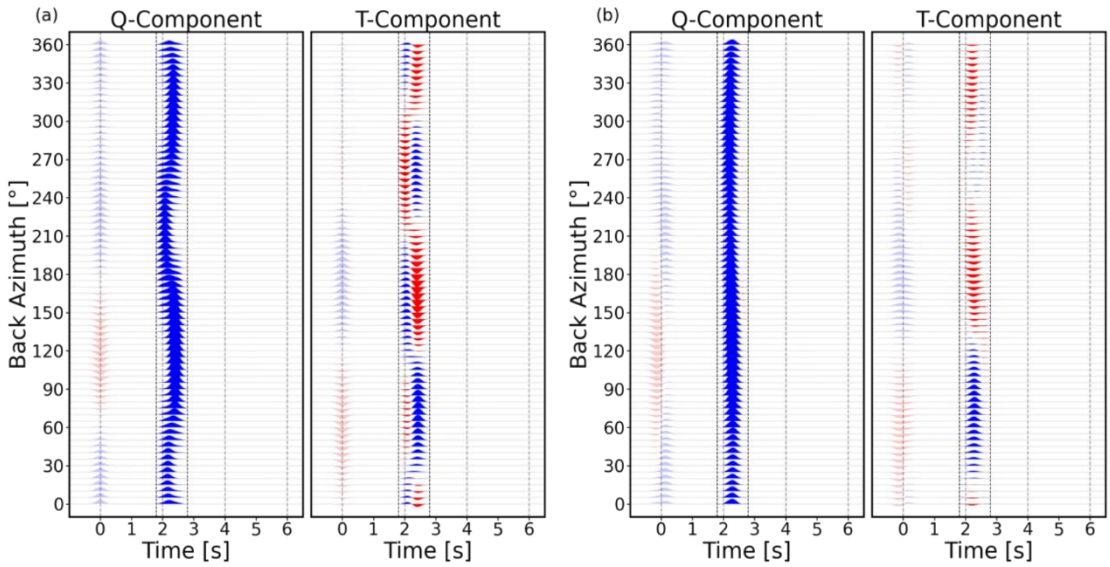

Figure 3. Receiver functions profile of synthetic test, (a) before and (b) after shear wave splitting correction. The phases used for the analysis were emphasized based on the time window. A two-layer model with a tilt interface and detailed assumed value are listed in Table 1.

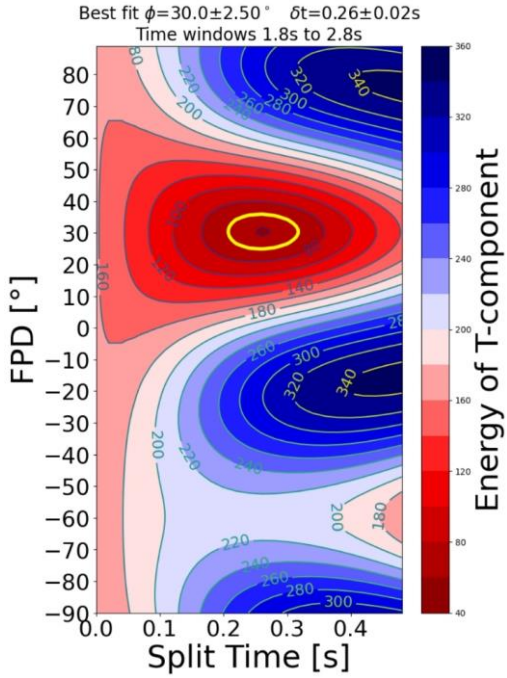

Figure 4. Grid search contour obtained from the synthetic test. The top of the panel shows the best fit parameter pair with standard error and the time window used for the analysis. The yellow line represents the 95% confidence interval.

3 Results

3.1 BIC in receiver function calculation

In the original time-domain iterative deconvolution method, the user was required to set a maximum iteration number and δε as conditional judgment. In this study, we applied BIC as an additional criterion of equal importance to δε. Figure 5 illustrates the variation curves of the sum of square error (SSE) and BIC value during the deconvolution process using observed data. The SSE value decreased as the iteration number increased, ultimately satisfying the conditional judgment and stopping the iteration. By contrast, the BIC value reached its minimum at an earlier iteration. By incorporating BIC, the number of spikes in both radial and tangential components was reduced by one-third to one-half compared to those using the traditional judgment condition, SSE. These results demonstrate the effectiveness of our approach in controlling the size of the resulting model while maintaining its reliability.

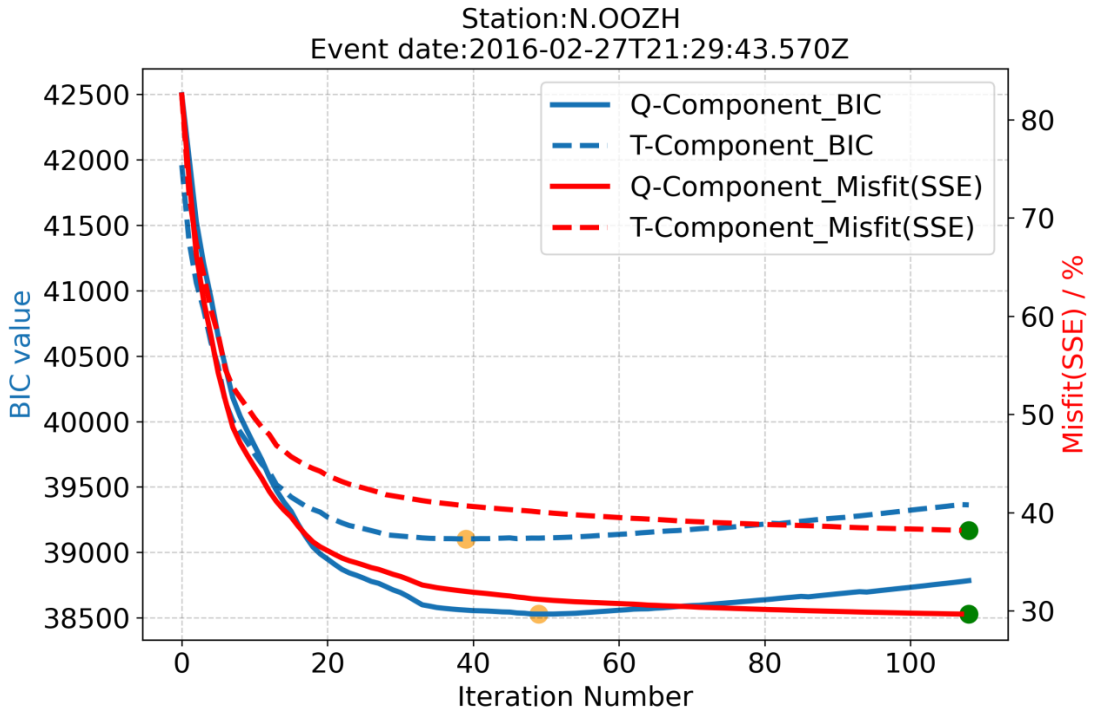

Figure 5. Variations of the BIC value and SSE value versus iteration number. Yellow dots indicate the minimum value in BIC curves. Green dots indicate where the iteration fits the SSE condition and stopped.

3.2 Receiver functions

Q-component RF traces exhibited primary phases with positive amplitudes, indicating the Mohorovičić discontinuity (Moho) in the slab. (Figure 6). At station N.OOZH, located in the western part along the MTL, clear positive phases appeared at ~5–6 s in the *Q*-component of the RFs, which were inferred as converted *Ps* phases from the slab Moho in the subducting PHS Plate. Similar positive phases appeared earlier, at ~3.5–4.5 s at station N.NAKH in the southwest part. This difference in the time lag of *Ps* phases is consistent with the geometry investigation of the PHS Plate by Shiomi et al. (2008).

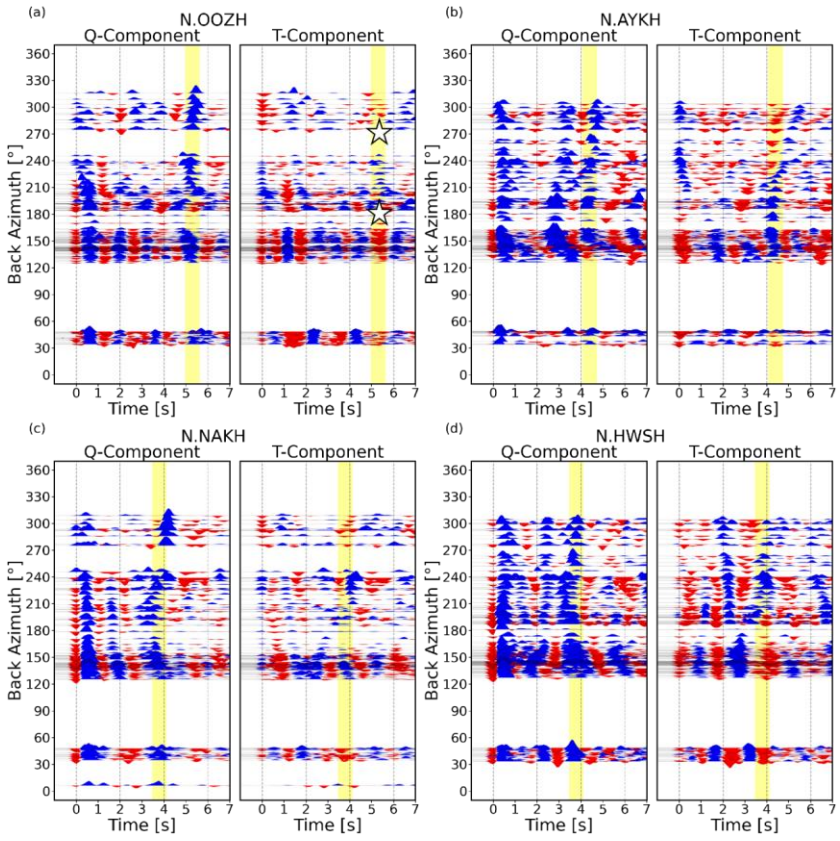

Figure 6. Examples of RFs obtained at the N.OOZH, N.NAKH, N.AYKH, and N.HWSH stations of NIED Hi-net. Station locations are shown in Figure 2. The vertical and horizontal axes represent the back-azimuth and time lag after *P* arrival, respectively. The RFs were grouped into 5° back-azimuthal bins. The blue area indicates the positive amplitude of each RF and the red area is the negative amplitude. The yellow lines indicate the arrival of the slab Moho-

converted phases estimated from the *Q*-component RFs at each station. The star symbols indicate the positions of changes in phase polarization.

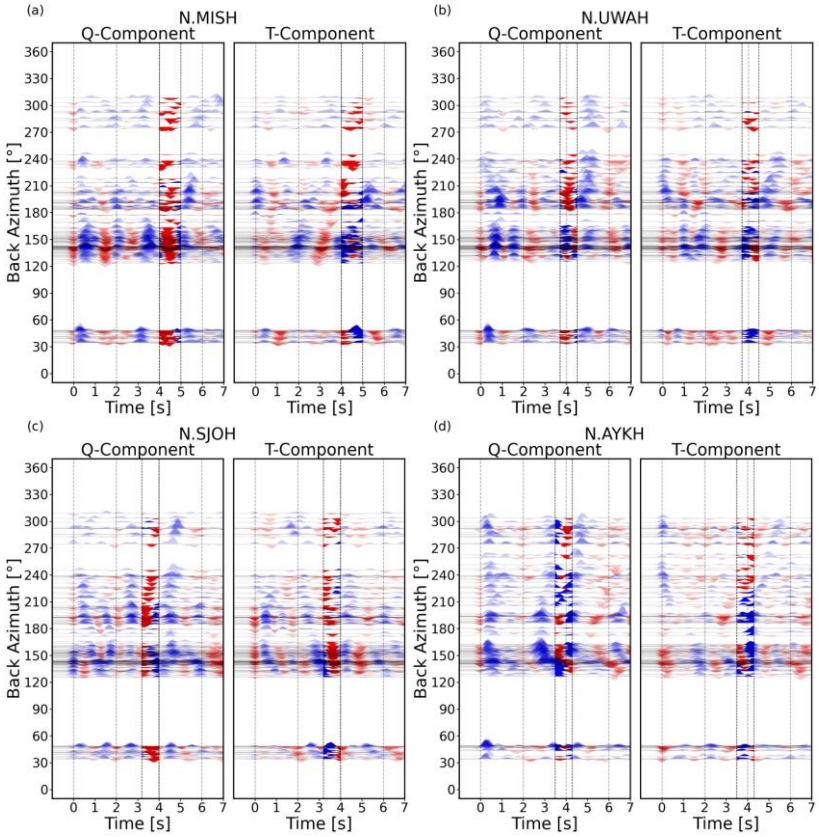

Figure 7. RF profiles from the station above the tectonic tremor-clustered area listed from west to east; (a) N.MISH, (b) N.UWAH, (c) N.SJOH, and (d) N.AYKH. The emphasized consistent negative phases just before the phases were converted from slab Moho indicate the existence of a relatively high-velocity layer.

We also observed phases in *T*-component RFs; however, these phases did not show a rigorous four-lobed pattern like an anisotropic horizontal layer at both stations. We found polarity reversals in the *T*-component RF phases, and the corresponding change in the polarization was also identified in the *Q*-component (Figure 6a). This approximately 90° back-azimuth interval in the *T*-component suggests the existence of a weak four-lobed pattern. This back-azimuthal pattern also reflects the combined effects of anisotropy and the dipping oceanic Moho. Clear positive phases from the Moho discontinuity in the *Q*-component of the RFs appeared at approximately 4 s (Figure 6c, d). We observed a series of coherent significant negative phases,

233 which may imply that the mantle wedge exists beneath the station, slightly earlier than the
234 positive converted phases from the slab Moho (Figure 7).

235 ***3.3 Anisotropic features revealed by splitting analysis***

236 Based on the anisotropic multi-layer assumption, we identified a series of distinct phases
237 that were consistently converted at the interface and contained all seismic anisotropic effects
238 above this interface. We focused on the anisotropic effects above the slab Moho: continental
239 crust (CC), mantle wedge (MT), and oceanic crust (OC), as shown in Figure 8. The FPD at each
240 station was calculated individually. These FPDs and delay times were estimated with an
241 acceptable standard error of $2\sigma \leq 20°$ (Shiomi et al., 2020). The results of the FPDs showed
242 different spatial characteristics between the southern and northern regions. In the south, the FPDs
243 show a NE–SW direction. By contrast, the FPDs in the north exhibited a tendency to rotate in the
244 slab plunge direction. Our study found that the azimuthal anisotropic fast axes changed from a
245 trench-parallel to a trench-normal direction in the southern area toward the northern part. This
246 change was strongly correlated with the dehydration and mineral evolution from the young and
247 hot PHS Plate subduction (Ji & Yoshioka, 2017; Horn et al., 2020; Lee & Kim, 2021). The
248 anisotropic strength was comparatively weaker along the tectonic tremor-clustered area,
249 especially in northwestern Shikoku Island, with an average split time of 0.057 s.

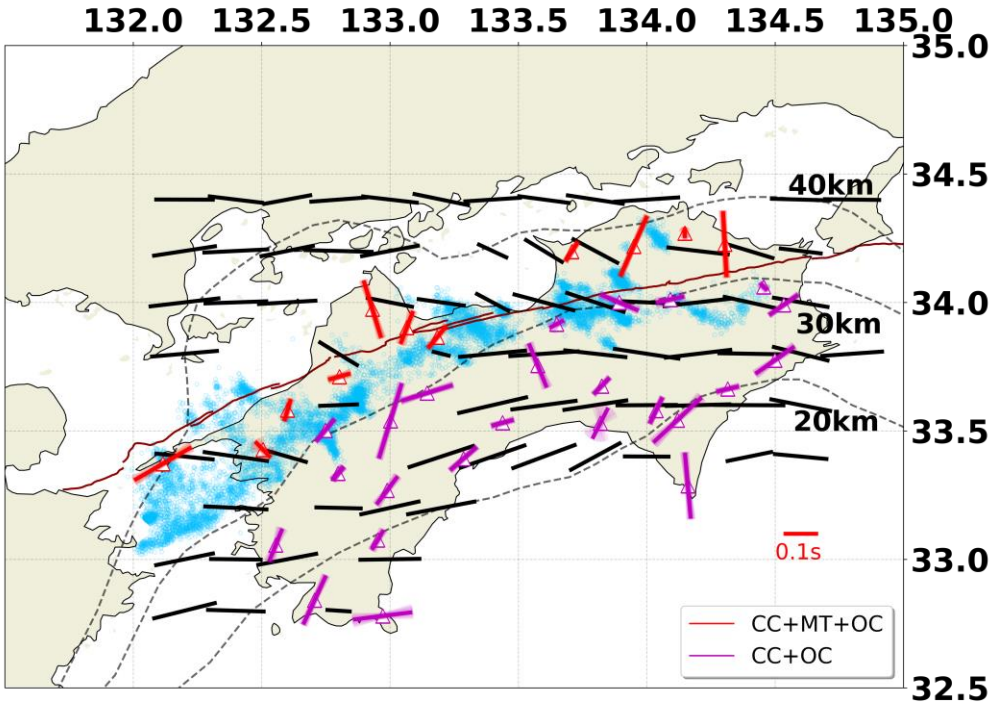

250 **Figure 8.** Distribution of FPDs in Shikoku district. The legend shows the splitting analysis
251 results from different anisotropic layers in the different color bars with light-color bars indicate
252 uncertainty. The black bars indicate the direction of normalized S_{hMax} (Uchide et al., 2022). The
253 sky-blue-colored circles indicate the distribution of tremors (Maeda & Obara, 2009; Obara et al.,
254 2010).

255 **4 Discussion**

256 ***4.1 Characteristics of receiver function***

257 Our observations of the slab Moho-converted phases in eastern Shikoku Island indicate
258 that these phases occur on average at a time of ~4–5 s, which is ~1 s earlier than in western
259 Shikoku Island, except for at the southernmost station N.MURH, where the phase occurs at ~3 s
260 (see Figure 9). Ito et al. (2009) reported that the slab in eastern Shikoku changes from a dip angle
261 of 6° to a steeper angle further north of the MTL. We therefore hypothesize that the relatively
262 constant arrival time of the slab Moho-converted phases in this area may be due to variations in
263 the thickness of the sedimentary layers, which become thinner toward the north. This hypothesis
264 is consistent with the results of a previous survey conducted by the Cabinet Office of Japan in

2018. The opposing effects of the later time lag resulting from a deeper slab Moho and the earlier time lag resulting from a thinner sedimentary thickness may cancel each other out, leading to the nearly identical arrival time of the slab Moho *Ps* phases. Our observations of the Moho slab in western Shikoku are consistent with previous studies (Nagaya et al., 2011; Shiomi et al., 2020). However, in eastern Shikoku, the variation in sedimentary thickness makes it challenging to determine the true depth of the Moho slab.

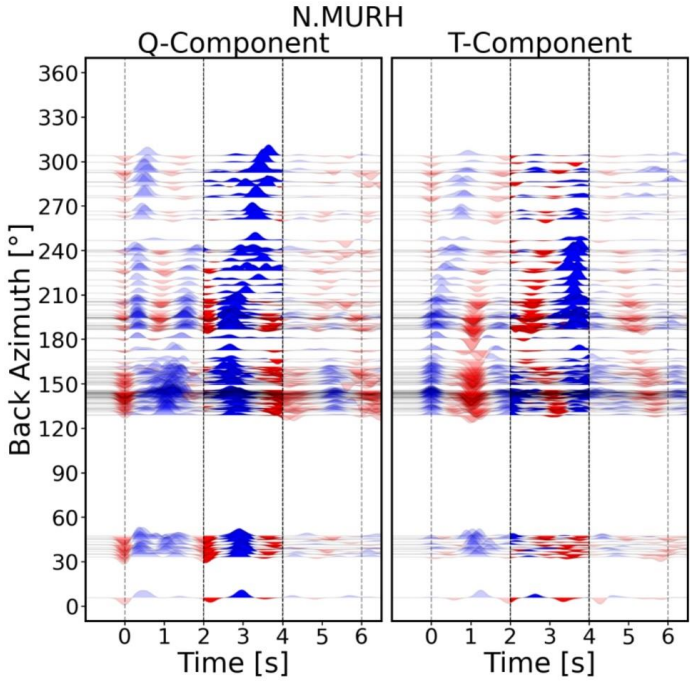

Figure 9. RF profiles obtained at the N.MURH station. The vertical and horizontal axes represent the back-azimuth and time lag after *P* arrival, respectively. The blue and red areas indicate positive and negative amplitude of amplitude of each RF, respectively. The highlighted positive phases at ~3 s indicate the phases converted from slab Moho.

Seismic multiples can have a significant impact on RFs, including methods like the H-κ stacking used to determine crustal thickness (Zhu & Kanamori, 2000). Additionally, reverberations from sedimentary layers can also affect RF analysis (Cunningham & Lekic, 2019; Yu et al., 2015; Zhang & Olugboji, 2021). A previous survey of Shikoku Island suggested that the top interface of the layer with a shear-wave velocity of ~3 km/s is located at a depth of 1.2–1.6 km in the northern part of the island and 1.6–2.5 km in the southern part (Cabinet Office Japan, 2018). When considering the existence of reverberations from sedimentary layers, it

becomes apparent that previous studies may have overestimated the anisotropic properties of Shikoku Island (Watanabe & Oda, 2015). This is because these studies treated the reverberations as converted phases from a comparatively deeper interface within the continental crust beneath the F-net stations on Shikoku Island, which may have resulted in an overemphasis on anisotropic strength deeper than the sedimentary layers themselves.

4.2 Anisotropic properties in the Shikoku Island

EDA remains a valuable tool for understanding crustal anisotropic features. Uchide et al. (2022) investigated crustal stress orientations in Japan using focal mechanism solutions from small earthquakes. Their results for Shikoku Island show that the local crustal S_{hMax} is oriented in the E–W to NE–SW direction to the south of the MTL. Our results show that FPDs are shifted in an iso-depth direction in most of the southern part of Shikoku Island (Figure 4) and may indicate that oriented fractures caused by bending-related faulting of the oceanic slab dominate the anisotropy direction (Faccenda et al., 2008). Moreover, the FPD results are consistent with the orientations of S_{hMax} around the MTL in eastern Shikoku Island. The highly oriented closure of fractures and microcracks by local stress can explain the results. On the other hand, to the north of the MTL, the orientations of the S_{hMax} are in the WNW–ESE direction. Meanwhile, our FPD results in this region showed a different plunging direction of the slab. The difference in direction in the northern part of Shikoku Island further suggests that the main contribution of shear-wave splitting is out of the crust in this area.

4.3 Thermal and hydrous condition in the northern part

The depth of the top surface of the PHS Plate corresponded to approximately 30–40 km in the northern area of Shikoku Island (Figure 4). The thermal gradient within the oceanic crust becomes larger at approximately 30 km or deeper, and the temperature is ~400–500 °C within the target depth of the PHS Plate (Yoshioka et al., 2008). The temperature distribution at 2.5 km above the PHS Plate surface was ~450–600 °C (Tatsumi et al., 2020). Commonly, chrysotile and lizardite are generated at 50–300 °C, transformed into antigorite at ~300–400 °C, and then stabilized at ~400–600 °C (Evans, 2010; Lafay et al., 2013). Tectonic tremors may be associated with the dehydration of the subducting oceanic crust during the thermal transition zone, where brittle deformation turns into ductile creep (Hyndman et al., 1995). According to Mizukami et al.

(2014), the progress of serpentinization and metasomatic reactions can result in a significant amount of residual water, leading to an increase in pore fluid pressure in SiO_2-rich fluid systems.

4.4 Tectonic tremor and serpentinite layer above the plate interface

Differences in tectonic tremor activity may be caused by lateral variations in pore fluid pressure and the mechanical strength of the hanging wall mantle. Our observations reveal a strong anisotropy with a delay time of 0.2 s in the N–S direction beneath the stations where the subducting slab plunges deeper and no tectonic tremors. This sub-parallel slab plunge is common in subduction zones are detected (Castellanos et al., 2020; Karato et al., 2008; Zhao et al., 2021). The lineation fabric (LPO) of olivine is likely generated by flow-induced strain within the mantle wedge (Nakajima & Hasegawa, 2004) and/or a serpentinized layer on the plate interface with low-angle subduction (Shiomi et al., 2020).

The observed FPDs along the iso-depth contours between 30 and 40 km depth, mainly around the sources of tectonic tremors, had an average delay time of 0.05 s and may reflect the degree of serpentinization of the mantle wedge (Figure 4). The observed strength and direction of FPDs are consistent with those in western Shikoku and the western Kii Peninsula (Saiga et al., 2013; Shiomi et al., 2020). The layered serpentinite above the plate interface within the wedge mantle exhibits the same strength of anisotropy as the olivine in the wedge mantle, which is ten times thicker than the serpentinite layer (Katayama et al., 2009). The serpentinized mantle wedge can host tectonic tremors and regulate slow-earthquake activity as well as coupling at the plate interface (Katayama et al., 2009, 2013). Furthermore, the dehydration of the oceanic crust results in the serpentinite layer on the plate interface generally growing above the plate interface at the corner of the mantle wedge (Lee & Kim, 2021).

We observed weaker anisotropy along the iso-depth contours across the tectonic tremor band (Figure 4) compared to other subduction zones with serpentinized layers, such as the Ryukyu subduction zone (Katayama et al., 2009). One explanation for this weaker anisotropy within the wedge mantle is the high fluid pressure conditions around the tectonic tremor sources. Fault weakening and shear failure caused by fluid overpressures from metasomatic reactions or serpentinization may disrupt the anisotropic features of foliate serpentine at the plate interface, particularly in regions with high excitation efficiency (Tarling et al., 2019). Additionally, Tang et al. (2015) suggested that anisotropic parameters decrease with increasing pore fluid saturation.

An alternative idea is a narrow-wedge mantle under low-angle subduction, where the tectonic tremor sources are distributed near the top of the mantle wedge with a thickness of a few kilometers (e.g., Sawaki et al., 2021; Shelly et al., 2006). In this case, a delay time <0.05 s in shear wave splitting is expected due to serpentine anisotropy (Katayama et al., 2009).

5 Conclusions

A combined analysis of the RF and shear-wave splitting revealed anisotropic features beneath Shikoku Island in southwestern Japan. In southern Shikoku, FPDs of the anisotropy are typically sub-parallel to the iso-depth contours of the top boundary of the PHS Plate, which possibly reflect the faults and the oceanic slab bending. In northern Shikoku, FPDs from the northeastern region rotate toward the slab plunge, indicating the existence of a serpentinized mantle wedge. However, in the region of the tectonic tremor-clusters, the anisotropic strength was lower, especially in the northwestern region of the island. We did not observe a strong anisotropic strength, although serpentine is present in this region under suitable thermal-hydrous conditions. The reduced anisotropic strength in the northwestern region of Shikoku Island may be due to hydrofracture and high pore fluid saturation, which can weaken the anisotropic strength of antigorite alone at the slab interface. To gain a deeper understanding of these factors and investigate the specific structure, we plan to use a more reliable Markov chain Monte Carlo-based inversion in our future studies.

Acknowledgements

Seismic analysis codes (Helffrich et al., 2013) and ObsPy (Beyreuther et al., 2010) were used to process waveform data. We are very grateful to Andrew Frederiksen and Jeffrey Park, also Audet Pascal and Bloch Wasja for their free-access codes. The figures in this study were drawn using Matplotlib (Hunter, 2007). This research was supported by JSPS KAKENHI (grant number 21H05203) as part of the Grant-in-Aid for Transformative Research Areas (A) “Science of Slow-to-Fast Earthquakes”, and the Ministry of Education, Culture, Sports, Science and Technology (MEXT) of Japan under its “The Second Earthquake and Volcano Hazards Observation and Research” Program (Earthquake and Volcano Hazard Reduction Research).

Data Availability Statement

The seismic records of Hi-net (National Research Institute for Earth Science and Disaster Resilience, 2019a) and F-net (National Research Institute for Earth Science and Disaster Resilience, 2019b) are available from the National Research Institute for Earth Science and Disaster Resilience Hi-net (https://www.hinet.bosai.go.jp/?LANG=en) and F-net (https://www.fnet.bosai.go.jp/top.php?LANG=en). The NIED tremor catalog is also available at the NIED Hi-net.

References

Annoura, S., Obara, K., & Maeda, T. (2016). Total energy of deep low-frequency tremor in the Nankai subduction zone, southwest Japan. *Geophysical Research Letters*, *43*(6), 2562–2567. https://doi.org/10.1002/2016GL067780

Audet, Pascal, & Bloch, Wasja. (2022, February 15). PyRaysum: Software for modeling ray-theoretical body-wave propagation. Zenodo. https://doi.org/10.5281/zenodo.6095749

Beyreuther, M., Barsch, R. Barsch, Krischer, L., Megies, Krischer, T. Megies, Behr, Y. Behr, & J. Wassermann (2010). ObsPy: A python toolbox for seismology. *Seismological Research Letters*, *81*(3), 530–533. https://doi.org/10.1785/gssrl.81.3.530

Cabinet Office Japan, Disaster Management. (2018). *Seismic intensity of inland earthquake in Chubu and Kinki: Data of surface soli* structure. Retrieved from: https://www.bousai.go.jp/jishin/chubu_kinki/syousai/pdf/sankousiryou3.pdf

Castellanos, J. C., Perry-Houts, J., Clayton, R. W., Kim, Y., Stanciu, A. C., Niday, B., & Humphreys, E. (2020). Seismic anisotropy reveals crustal flow driven by mantle vertical loading in the Pacific NW. *Science Advances*, *6*(28), eabb0476. https://doi.org/10.1126/sciadv.abb0476

Crampin, S., Evans, R., & Atkinson, B. K. (1984). Earthquake prediction: A new physical basis. *Geophysical Journal International*, *76*(1), 147–156. https://doi.org/10.1111/j.1365-246X.1984.tb05030.x

Crampin, S., & Peacock, S. (2005). A review of shear-wave splitting in the compliant crack-critical anisotropic Earth. *Wave Motion*, *41*(1), 59–77. https://doi.org/10.1016/j.wavemoti.2004.05.006

Cunningham, E., & Lekic, V. (2019). Constraining crustal structure in the presence of sediment: A multiple converted wave approach. *Geophysical Journal International*, *219*(1), 313–327. https://doi.org/10.1093/gji/ggz298

Evans, B. W. (2010). Lizardite versus antigorite serpentinite: Magnetite, hydrogen, and life(?). *Geology*, *38*(10), 879–882. https://doi.org/10.1130/G31158.1

Frederiksen, A. W., & Bostock, M. G. (2000). Modelling teleseismic waves in dipping anisotropic structures. *Geophysical Journal International*, *141*(2), 401–412. https://doi.org/10.1046/j.1365-246x.2000.00090.x

Helffrich, G., Wookey, J. & Bastow, I. (2013). The seismic analysis code. https://doi.org/10.1017/cbo9781139547260

Hess, H. H. (1964). Seismic anisotropy of the uppermost mantle under oceans. *Nature*, *203*(4945), 629–631. https://doi.org/10.1038/203629a0

Hirose, F., Nakajima, J., & Hasegawa, A. (2008). Three-dimensional seismic velocity structure and configuration of the Philippine Sea slab in southwestern Japan estimated by double-difference tomography. *Journal of Geophysical Research: Solid Earth*, *113*(B9), B09315. https://doi.org/10.1029/2007JB005274

Horn, C., Bouilhol, P., & Skemer, P. (2020). Serpentinization, deformation, and seismic anisotropy in the subduction mantle wedge. *Geochemistry, Geophysics, Geosystems*, *21*(4), e2020GC008950. https://doi.org/10.1029/2020GC008950

Huang, Z., Zhao, D., & Wang, L. (2011). Shear wave anisotropy in the crust, mantle wedge, and subducting Pacific slab under northeast Japan. *Geochemistry, Geophysics, Geosystems*, *12*(1), Q01002. https://doi.org/10.1029/2010GC003343

Hunter, J. D. (2007). Matplotlib: A 2D graphics environment, *Computing in Science and Engineering*, *9*(3), 90–95, https://doi.org/10.1109/MCSE.2007.55

Hyndman, R. D., & Wang, K. (1995). The rupture zone of Cascadia great earthquakes from current deformation and the thermal regime. *Journal of Geophysical Research: Solid Earth*, *100*(B11), 22133–22154. https://doi.org/10.1029/95JB01970

Iidaka, T., Muto, J., Obara, K., Igarashi, T., & Shibazaki, B. (2014). Trench-parallel crustal anisotropy along the trench in the fore-arc region of Japan: Trench-parallel anisotropy along Japan. *Geophysical Research Letters*, *41*(6), 1957–1963. https://doi.org/10.1002/2013GL058359

Ishise, M., & Oda H. (2009). Anisotropic velocity structure of seismic waves in Japan subduction zone (in Japanese with English abstract). *Zisin (Journal of the Seismological Society of Japan. 2nd ser.)*, *61*(Supplement), 187–197. https://doi.org/10.4294/zisin.61.187

Ito, T., Kojima, Y., Kodaira, S., Sato, H., Kaneda, Y., Iwasaki, T., et al. (2009). Crustal structure of southwest Japan, revealed by the integrated seismic experiment Southwest Japan 2002. *Tectonophysics*, *472*(1–4), 124–134. https://doi.org/10.1016/j.tecto.2008.05.013

Ji, Y., & Yoshioka, S. (2017). Slab dehydration and earthquake distribution beneath southwestern and central Japan based on three-dimensional thermal modeling: Slab Dehydration in SW and Central Japan. *Geophysical Research Letters*, *44*(6), 2679–2686. https://doi.org/10.1002/2016GL072295

Karato, S., Jung, H., Katayama, I., & Skemer, P. (2008). Geodynamic significance of seismic anisotropy of the upper mantle: New insights from laboratory studies. *Annual Review of Earth and Planetary Sciences*, *36*(1), 59–95. https://doi.org/10.1146/annurev.earth.36.031207.124120

Katayama, I., Hirauchi, K.-ichi, Michibayashi, K., & Ando, J.-ichi. (2009). Trench-parallel anisotropy produced by serpentine deformation in the hydrated mantle wedge. *Nature*, *461*(7267), 1114–1117. https://doi.org/10.1038/nature08513

Katayama, I., Iwata, M., Okazaki, K., & Hirauchi, K. (2013). Slow earthquakes associated with fault healing on a serpentinized plate interface. *Scientific Reports*, *3*(1), 1784. https://doi.org/10.1038/srep01784

Lafay, R., Deschamps, F., Schwartz, S., Guillot, S., Godard, M., Debret, B., & Nicollet, C. (2013). High-pressure serpentinites, a trap-and-release system controlled by metamorphic conditions: Example from the Piedmont zone of the western Alps. *Chemical Geology*, *343*, 38–54. https://doi.org/10.1016/j.chemgeo.2013.02.008

Lassak, T. M., Fouch, M. J., Hall, C. E., & Kaminski, É. (2006). Seismic characterization of mantle flow in subduction systems: Can we resolve a hydrated mantle wedge? *Earth and Planetary Science Letters*, *243*(3–4), 632–649. https://doi.org/10.1016/j.epsl.2006.01.022

Lee, C., & Kim, Y. (2021). Role of warm subduction in the seismological properties of the forearc mantle: An example from southwest Japan. *Science Advances*, *7*(28), eabf8934. https://doi.org/10.1126/sciadv.abf8934

461 Ligorría, J. P., & Ammon, C. J. (1999). Iterative deconvolution and receiver-function estimation.
462 *Bulletin of the Seismological Society of America*, *89*(5), 1395–1400.
463 https://doi.org/10.1785/BSSA0890051395
464 Maeda, T., & Obara, K. (2009). Spatiotemporal distribution of seismic energy radiation from
465 low-frequency tremor in western Shikoku, Japan. *Journal of. Geophysical. Research: Solid*
466 *Earth*, 114, B00A09. https://doi.org/10.1029/2008JB006043
467 Mizukami, T., Yokoyama, H., Hiramatsu, Y., Arai, S., Kawahara, H., Nagaya, T., & Wallis, S.
468 R. (2014). Two types of antigorite serpentinite controlling heterogeneous slow-slip
469 behaviours of slab–mantle interface. *Earth and Planetary Science Letters*, *401*, 148–158.
470 https://doi.org/10.1016/j.epsl.2014.06.009
471 Nagaya, M., Oda, H., & Kamimoto, T. (2011). Regional variation in shear-wave polarization
472 anisotropy of the crust in southwest Japan as estimated by splitting analysis of Ps-converted
473 waves on receiver functions. *Physics of the Earth and Planetary Interiors*, *187*(1–2), 56–65.
474 https://doi.org/10.1016/j.pepi.2011.04.016
475 Nakajima, J., & Hasegawa, A. (2004). Shear-wave polarization anisotropy and subduction-
476 induced flow in the mantle wedge of northeastern Japan. *Earth and Planetary Science*
477 *Letters*, *225*(3–4), 365–377. https://doi.org/10.1016/j.epsl.2004.06.011
478 Nakanishi, A., Takahashi, N., Yamamoto, Y., Takahashi, T., Ozgur Citak, S., Nakamura, T. et al.
479 (2018). Three-dimensional plate geometry and P-wave velocity models of the subduction
480 zone in SW Japan: Implications for seismogenesis. *Geology and Tectonics of Subduction*
481 *Zones*: *A Tribute to Gaku Kimura*. https://doi.org/10.1130/2018.2534(04)
482 National Research Institute for Earth Science and Disaster Resilience (2019a). NIED Hi-Net,
483 National Research Institute for Earth Science and Disaster Resilience.
484 https://doi.org/10.17598/nied.0003
485 National Research Institute for Earth Science and Disaster Resilience (2019b). NIED F-net,
486 National Research Institute for Earth Science and Disaster Resilience.
487 https://doi.org/10.17598/nied.0005
488 Obara, K. (2002). Nonvolcanic deep tremor associated with subduction in Southwest Japan.
489 *Science*, *296*(5573), 1679–1681. https://doi.org/10.1126/science.1070378
490 Obara, K., & Kato, A. (2016). Connecting slow earthquakes to huge earthquakes. *Science*,
491 *353*(6296), 253–257. https://doi.org/10.1126/science.aaf1512

Obara, K., Tanaka, S., Maeda, T., & Matsuzawa, T. (2010). Depth-dependent activity of non-volcanic tremor in southwest Japan. *Geophysical Research Letters*, 37(13), L13306. https://doi.org/10.1029/2010GL043679

Saiga, A., Kato, A., Kurashimo, E., Iidaka, T., Okubo, M., Tsumura, N., et al. (2013). Anisotropic structures of oceanic slab and mantle wedge in a deep low-frequency tremor zone beneath the Kii Peninsula, SW Japan: Anisotropic structure around LFE zone. *Journal of Geophysical Research: Solid Earth*, *118*(3), 1091–1097. https://doi.org/10.1002/jgrb.50069

Sawaki, Y., Ito, Y., Ohta, K., Shibutani, T., & Iwata, T. (2021). Seismological structures on bimodal distribution of deep tectonic tremor. *Geophysical Research Letters*, *48*(8), e2020GL092183. https://doi.org/10.1029/2020GL092183

Schwarz, G. (1978). Estimating the dimension of a model. *The Annals of Statistics*, *6*(2), 461–464. https://doi.org/10.1214/aos/1176344136

Seno, T., Stein, S., & Gripp, A. E. (1993). A model for the motion of the Philippine Sea Plate consistent with NUVEL-1 and geological data. *Journal of Geophysical Research: Solid Earth*, *98*(B10), 17941–17948. https://doi.org/10.1029/93JB00782

Shelly, D. R., Beroza, G. C., Ide, S., & Nakamula, S. (2006). Low-frequency earthquakes in Shikoku, Japan, and their relationship to episodic tremor and slip. *Nature*, *442*(7099), 188–191. https://doi.org/10.1038/nature04931

Shiomi, K. (2013). New measurements of sensor orientation at NIED Hi-net stations (in Japanese with English abstract). *Report of the National Research Institute for Earth Science and Disaster Resilience*, 80, 1–20. http://doi.org/10.24732/nied.00001219

Shiomi, K., Matsubara, M., Ito, Y., & Obara, K. (2008). Simple relationship between seismic activity along Philippine Sea slab and geometry of oceanic Moho beneath southwest Japan. *Geophysical Journal International*, *173*(3), 1018–1029. https://doi.org/10.1111/j.1365-246X.2008.03786.x

Shiomi, K., Obara, K., & Sato, H. (2006). Moho depth variation beneath southwestern Japan revealed from the velocity structure based on receiver function inversion. *Tectonophysics*, *420*(1–2), 205–221. https://doi.org/10.1016/j.tecto.2006.01.017

Shiomi, K., & Park, J. (2008). Structural features of the subducting slab beneath the Kii Peninsula, central Japan: Seismic evidence of slab segmentation, dehydration, and

anisotropy. *Journal of Geophysical Research: Solid Earth*, *113*(B10), B10318. https://doi.org/10.1029/2007JB005535

Shiomi, K., Takeda, T., & Ueno, T. (2020). Seismological evidence of a dehydration reaction in the subducting oceanic crust beneath western Shikoku in southwest Japan. *Geophysical Journal International*, *224*(1), 151–168. https://doi.org/10.1093/gji/ggaa423

Silver, P. G., & Chan, W. W. (1991). Shear wave splitting and subcontinental mantle deformation. *Journal of Geophysical Research: Solid Earth*, *96*(B10), 16429. https://doi.org/10.1029/91JB00899

Tang, J., Fang, B., Sun, C., & Shao, J. (2015). Study of seismic wave propagation characteristics based on anisotropic fluid substitution in fractured medium. *Geophysical Prospecting for Petroleum*, *54*(1), 1–8. https://doi.org/10.3969/j.issn.1000-1441.2015.01.001

Tarling, M. S., Smith, S. A. F., & Scott, J. M. (2019). Fluid overpressure from chemical reactions in serpentinite within the source region of deep episodic tremor. *Nature Geoscience*, *12*(12), 1034–1042. https://doi.org/10.1038/s41561-019-0470-z

Tatsumi, Y., Suenaga, N., Yoshioka, S., Kaneko, K., & Matsumoto, T. (2020). Contrasting volcano spacing along SW Japan arc caused by difference in age of subducting lithosphere. *Scientific Reports*, *10*(1), 15005. https://doi.org/10.1038/s41598-020-72173-6

Uchide, T., Shiina, T., & Imanishi, K. (2022). Stress map of Japan: Detailed nationwide crustal stress field inferred from focal mechanism solutions of numerous microearthquakes. *Journal of Geophysical Research: Solid Earth*, *127*(6), e2022JB024036. https://doi.org/10.1029/2022JB024036

Ueno, T., Shibutani, T., & Ito, K. (2008). Subsurface structures derived from receiver function analysis and relation to hypocenter distributions in the region from the eastern Shikoku to the northern Chugoku districts, Southwest Japan. *Earth, Planets and Space*, *60*(6), 573–579. https://doi.org/10.1186/BF03353120

United States Geological Survey. (2022). Advanced National Seismic System (ANSS) Comprehensive Catalog. United States Geological Survey. https://doi.org/10.5066/F7MS3QZH

Walsh, E., Arnold, R., & Savage, M. K. (2013). Silver and Chan revisited. *Journal of Geophysical Research: Solid Earth*, *118*(10), 5500–5515. https://doi.org/10.1002/jgrb.50386

554 Wang, J., Huang, X., Zhao, D., & Yao, Z. (2019). Seismic anisotropy evidence for ductile
555 deformation of the forearc lithospheric mantle in subduction zones. *Journal of Geophysical*
556 *Research: Solid Earth*, *124*(7), 7013–7027. https://doi.org/10.1029/2018JB016912
557 Watanabe, M., & Oda, H. (2015). Shear-wave anisotropy of the upper and lower crusts estimated
558 by stripping analysis of Ps-converted waves. *Tectonophysics*, *658*, 137–150.
559 https://doi.org/10.1016/j.tecto.2015.07.016
560 Yoshioka, S., Toda, M., & Nakajima, J. (2008). Regionality of deep low-frequency earthquakes
561 associated with subduction of the Philippine Sea plate along the Nankai Trough, southwest
562 Japan. *Earth and Planetary Science Letters*, *272*(1–2), 189–198.
563 https://doi.org/10.1016/j.epsl.2008.04.039
564 Yu, Y., Song, J., Liu, K. H., & Gao, S. S. (2015). Determining crustal structure beneath seismic
565 stations overlying a low-velocity sedimentary layer using receiver functions. *Journal of*
566 *Geophysical Research: Solid Earth*, *120*(5), 3208–3218.
567 https://doi.org/10.1002/2014JB011610
568 Zhang, Z., & Olugboji, T. (2021). The signature and elimination of sediment reverberations on
569 submarine receiver functions. *Journal of Geophysical Research: Solid Earth*, *126*(5),
570 e2020JB021567. https://doi.org/10.1029/2020JB021567
571 Zhao, D., Wang, J., Huang, Z., & Liu, X. (2021). Seismic structure and subduction dynamics of
572 the western Japan arc. *Tectonophysics*, *802*, 228743.
573 https://doi.org/10.1016/j.tecto.2021.228743
574 Zhu, L., & Kanamori, H. (2000). Moho depth variation in southern California from teleseismic
575 receiver functions. *Journal of Geophysical Research: Solid Earth*, *105*(B2), 2969–2980.
576 https://doi.org/10.1029/1999JB900322